Exploring The Anion Chemical Space: A Model of Electroelastic Material $Ln_2OF_{2-x}Cl_xH_2$ (Ln=Y,La,Gd) with High Mechanical Sensitivity and Remarkable Energy Harvesting

Evgenii Strugovshchikov* and Aleksandr Pishtshev

Institute of Physics, University of Tartu, W.Ostwaldi 1, 50411 Tartu, Estonia.

E-mail: evgenii.strugovshchikov@ut.ee,aleksandr.pishtshev@ut.ee

Abstract

The main result of our investigation is the prediction of a new family of multi-anion compounds – $Ln_2OF_{2-x}Cl_xH_2$ (Ln=Y,La,Gd) which due to anomalous elastic behaviour could present interest for the design and development of electromechanical devices. The composition $Ln_2OF_{2-x}Cl_xH_2$ utilizes complex heteroatomic anion $[OF_{2-x}Cl_xH_2]^{6-}$; in a solid state, as it follows from the DFT calculations, the system crystallizes into a columnar-type layered structure of $P3m1$ or $R3m$ trigonal symmetries in which the LnO(F,Cl)H and Ln(F,Cl)FH layers are uniformly stacked in an alternating order along the high-symmetry c axis. In the trigonal lattice without inversion center, the resulting two-layers geometry puts groups of the anionic species together in a way that gives rise to the strong localization of valence charge density. We showed that being globally stable, such specific crystal architecture may lead to a high asymmetry of mechanical and electrical responses with respect to imposed loads. Moreover, small dynamic changes of the equilibrium charge and bonding configurations may cause rather the enhanced structural sensitivity of elastic responses at low pressures. Comparison of electromechanical characteristics showed that the predicted materials can serve as direct successors of the line of PVDF piezopolymers.

Introduction

Recently, there has been a significant interest in investigation of a series of mixed-anion inorganic compounds.[1,2] Classic examples are condensed oxyhydrides[3–10] and oxyfluorides;[11–14] they are of peculiar interest to the development of new generation of perspective functional materials. As it was reported in a number of the experimental and theoretical studies of bulk phases of yttrium oxyhydrides,[15–19] the anionic nature of these compounds is such that in the condensation process one can flexibly control structural, elastic and charge degrees of freedom by manipulating anion configurations in terms of O/H ratio. From both fundamental and applied points of view, the possibility to manage structure-property relationships provides a promising opportunity to create the desired functionality by utilizing the proper properties determined by the anionic framework of the given oxyhydride composition. In particular, it was repeatedly demonstrated[15,20,21] that thin solid films developed from several rare-earth metal oxyhydrides exhibit a light-induced change of the intrinsic color in the visible region (photochromism phenomenon). In our previous work,[18] based on the advanced DFT calculations, we have analysed how structural and electronic properties of a solid oxyhydride can be tuned through the change of the oxygen content and coordinations in crystal lattices of different symmetries. The obtained results allowed us to predict the whole class of polar yttrium and lanthanum oxyhydride systems Ln_2H_4O (Ln=Y,La) with strong ferro- and piezoelectric properties.[19]

According to our theoretical studies of the $[H_xO_y]^{-(x+2y)}$ structural chemistry, one of the crucial features of a condensed mixed-anion system is dynamic character of the equilibrium chemical configuration. This feature is also connected with its global stability which becomes directly dependent on how different anions share the common part of chemical space. As the distribution of the anions in the three-dimensional lattice readily responds to any change of the anion composition, the objective of the present work is to determine in which degree such change of the crystal-chemical environment influences the physical responses the oxyhydride system displays to external action.

Table 1: Models of the crystallization of the $Ln_2OF_{2-x}Cl_xH_2$ compounds. The '+' sign means that the structure is stable for the given composition. The $P3m1$ phase has the lowest energy and is chosen as a reference point. ΔE denotes the energy barrier between $P3m1$ and $R3m$ crystalline phases.

X	Chem. formula	Structure $P3m1$	Structure $R3m$	ΔE (kJ/mol)	Chem. formula	Structure $P3m1$	Structure $R3m$	ΔE (kJ/mol)	Chem. formula	Structure $P3m1$	Structure $R3m$	ΔE (kJ/mol)
0	$Y_2OF_2H_2$	+	+	+12.7	$La_2OF_2H_2$	+	+	+11.0	$Gd_2OF_2H_2$	+	+	+13.8
1	Y_2OFClH_2	+	+	+3.7	La_2OFClH_2	+	+	+7.6	Gd_2OFClH_2	+	+	+5.1
					$LaGdOFClH_2$	+	+	+6.3				
2	$Y_2OCl_2H_2$	−	+	−	$La_2OCl_2H_2$	−	+	−	$Gd_2OCl_2H_2$	−	+	−

In past years, the effect of anion substitutions in hydrogen containing systems has been already considered.[22] The idea to improve the potential of hydrides as a hydrogen storage system has been studied by performing the partial substitutions of H^- for F^-.[23–25] In the context of anionic specificity of metal oxyhydride, this fact stimulated us to investigate in which way the hydride ion may be displaceable by halogen. In particular, we would expect that the fluoride anion having larger electronegativity and smaller ionic radius in comparison with hydrogen could induce different redistributions of valence charge localization in the unit cell. In the present work, we simulated the substitution chemistry of the heteroatomic anion $[H_xO_y]^{-(x+2y)}$ in terms of the oxidative partial halogenation of the model oxyhydride Ln_2H_4O (Ln=Y, La). Fluoro-chloro variations of the oxyhydride system were modeled via selective replacing of a hydride ion by the isovalent negative-charged fluorine and chlorine anions. To unravel how halogen atom is incorporated into the hydrogen positions of the host structure, the $R3m$ phase of the bulk Ln_2H_4O (Ln=Y, La)[19] has been taken as a starting point. The choice of the $R3m$ crystal lattice was conditioned by its good structural stability and relatively simple layered geometry. Our principal interest was to gain an insight into the role of substituent in the modification of such bulk properties as elastic characteristics and the structural factors responsible for the lattice stability. The stability problem is of special attention because redistribution of valence electron density between three anions, induced by the substitution effect, may lead to softening of bonding forces. It should be

noted that the general scheme of expanding of anionic complexity has been earlier suggested for perovskite-like layered architectures through the increase of two-dimensional layers of octahedra-sharing vertices.[26–29] Next note that, based on the recent results on oxyfluoride layered systems like potassium beryllium fluoroborate $KBe_2BO_3F_2$,[30] one can expect various effects of strong elastic anisotropy in the substituted oxyhydrides. Moreover, the detail study of elastic behavior features attracts more interest as it can provide a conceptual design of the prospective lead-free dielectric with the potential that could effectively embody useful functionality of both relaxor ferroelectrics and electroactive soft polymers.

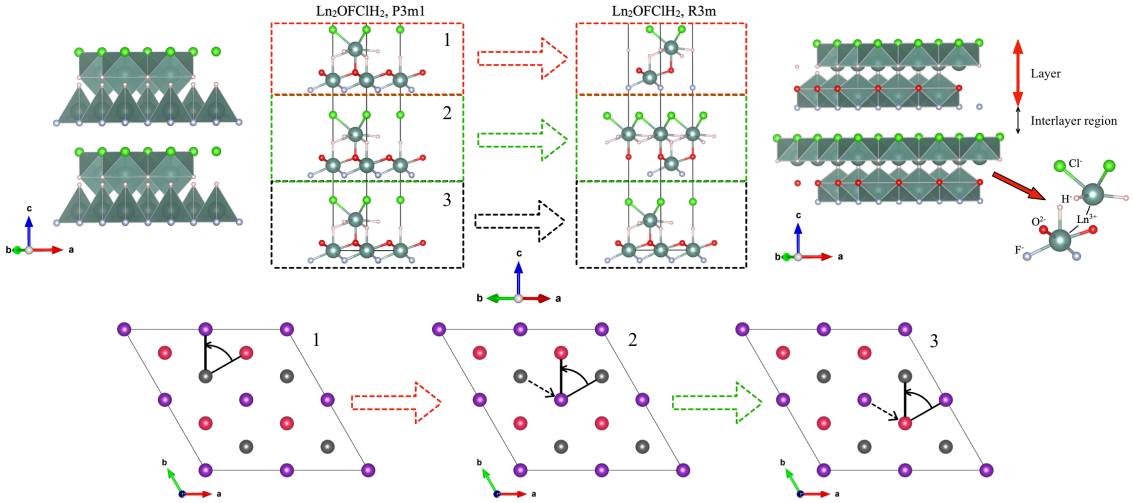

Figure 1: Illustrative model of three-dimensional close-packing for the $P3m1$ and $R3m$ phases of the bulk Ln_2OFClH_2. The model is drawn in terms of a charged heteroatomic layers $LnHCl^{+1}$ and $LnOF^{-1}$ stacked over each other. Yttrium, oxygen, hydrogen, chlorine and fluorine atoms are indicated by dark green, red, pink, green and pearl balls, respectively. The mechanism of polymorphic reconstruction is represented schematically in terms of shifts and rotation of atomic layers in the $[1\bar{1}0]$ crystallographic direction.

Computational and modeling details

Numerical simulations of theoretical models were based on density functional theory (DFT) calculations for which the generalized gradient approximation (GGA) with the Perdew–Burke –Ernzerhof (PBE) exchange-correlation functional[31] and plane-wave basis have been used.

The Vienna Ab-initio Simulation Package (VASP)[32,33] along with the projector augmented-wave (PAW) method[34,35] were employed for the computational work. The PAW pseudo-potentials for Y, La, Gd, O, F, Cl and H elements included the following valence electron configurations: $4s^2 4p^6 5s^2 4d^1$, $5s^2 5p^6 4f^0 6s^2 5d^1$, $5s^2 5p^6 4f^7 6s^2 5d^1$, $2s^2 2p^4$, $2s^2 2p^5$, $3s^2 3p^5$ and $1s^1$, respectively. All the calculations were performed with a cutoff energy of 700 eV and Brillouin-zone **k**-point sampling represented by a Γ-centered $8 \times 8 \times 8$ grid. The relaxed crystal geometries were obtained with a force criterion of 0.001 eV/Å. Using the Dudarev approach,[36] we took into account strong on-site correlations for La and Gd cations in terms of GGA + U_{eff} scheme. The Hubbard correction U_{eff} associated with the $4f$ atomic shell was chosen 5.5 and 4.6 eV for La and Gd, respectively.[37] To study topology properties of valence charge density distributions the electron localization function (ELF)[38,39] was used as an electronic descriptor for post-processing our calculations. The visualization of lattice geometries and ELF patterns were made by means of the Vesta program.[40]

We decided to choose the C_{3v} phase of yttrium oxyhydride Y_2H_4O as the starting point for our structural modeling. This choice allowed us to take into account several crystallographic factors specific to the condensed state of the two-anion compound; the most important are (i) the layer character of lattice geometry which is responsible for a high level of the elastic anisotropy, (ii) the simple lattice skeleton formed by the distribution of the atoms over $3a$ Wyckoff positions, and (iii) the Lewis basicity of the hydrogen, which governs the channel of strong localization of valence charge density. The halogenation process of the oxyhydride model $Ln_2H_4O \xrightarrow{\text{F \& Cl}} Ln_2H_2OF_{2-x}Cl_x$ was further simulated via the partial replacement of hydrogen in the $3a$ sites of the $R3m$ crystal lattice. Simulations of the crystal structure as an elastic body was made by using of the ELATE online tool.[41,42] The bulk modulus was calculated via the reciprocal of the volume compressibility.[43] The Debye temperature Θ_D has been evaluated within the frameworks of semi-empirical approach.[44] The values of Vickers hardness H_V have been estimated from the Mazhnik and Oganov model.[45] The theory-group analysis of model structures used the program tools[46,47] hosted by Bilbao Crystallographic

Server.[48–51] The thermodynamic stability of the oxyhydride models was evaluated in two ways: (i) calculation of the standard formation enthalpy ΔH with respect to such ingredients as Y, $1/2H_2$, $1/2F_2$, $1/2Cl_2$ and $1/2O_2$, and (ii) analysis of the energetics of reactions associated with the decomposition of $Ln_2H_2OF_{2-x}Cl_x$ into a mixture of different phases:

$$\frac{1}{3}\left(Ln_2O_3 + 2\,LnH_3 + (2{-}x)LnF_3 + xLnCl_3\right), \tag{1a}$$

$$\frac{1}{3}\left(3\,LnHO + LnH_3 + (2{-}x)LnF_3 + xLnCl_3\right). \tag{1b}$$

The dielectric and piezoelectric properties have been simulated by using numerical procedures of density functional perturbation theory.[52] For the characterization of deformable electroelastic solid we rested upon the following scheme:[53,54] The harvesting power $\mathcal{P}$ of piezoelectric element under displacement excitation:

$$\mathcal{P} = \frac{1}{2}\frac{I^2}{R} = \frac{1}{2}\frac{I}{\omega C} I\,Z = \frac{1}{2}\frac{\alpha X}{C}(\alpha\,\omega\,X)\,Z = \frac{1}{2}Z\,(\frac{\alpha_e}{C_p})^2\,(\omega\,C_p)\,X^2\,, \tag{2}$$

where α_e is force-voltage coupling factor, C_p is piezoelectric clamped capacitance, Z is the equivalent impedance of the outer electrical circuit and X is the magnitude of displacement in direction of applied pressure. The open-circuit piezoelectric voltage V_{OC} generated under displacement excitation:

$$V_{OC} = g_{33}\,P\,h = g_{33}\,E_z\,X\,, \tag{3}$$

where g_{33} is a piezoelectric voltage coefficient, P is a pressure applied in z direction, h is a thickness of the film, and E_z is a z-component of Young's modulus. From the equation $V_{OC} = \frac{\alpha_e}{C_p} X$ one obtains a final formula for $\mathcal{P}$:

$$\mathcal{P} = \frac{1}{2}Z\,(g_{33}\,E_z)^2\,(\omega\,C_p)\,X^2\,. \tag{4}$$

The first part of (4) characterizes the electromechanical features of the material, the second one measures response to the external impact in terms of the displacement X in the

direction of applied pressure. Coupling coefficient k_t for a pure thickness mode (no lateral deformations) is given by the expression:[55,56]

$$k_t{}^2 = \frac{e_{33}{}^2}{C_{33}{}^D \, \epsilon_{33}{}^S} \,, \tag{5}$$

where stiffness constant $C_{33}{}^D$ accounts for the piezoelectric contribution into stiffness $C_{33}{}^E$ at the constant E-field:

$$C_{33}{}^D = C_{33}{}^E + \frac{e_{33}{}^2}{\epsilon_{33}{}^S} \,. \tag{6}$$

Results and discussion

Crystallographic models

In Tables 1 – 2 and Figures 1 – 3 we presented the main results on the substitution effect in terms of structural modeling of the $\mathrm{H} \rightarrow \mathrm{F}, \mathrm{Cl}$ partial replacement. Additional information on details of lattice structure, elastic characteristics, and stability of $Ln_2OF_{2-x}Cl_xH_2$ stoichiometric compositions can be found in Tables S1 – S45 of ESI for Ln=Y,La,Gd.

Crystal chemical properties

As our modeling confirmed, the composition $Ln_2OF_{2-x}Cl_xH_2$ (Ln=Y,La,Gd) crystallizes in the C_{3v} polar structure that realizes either in the $R3m$ or $P3m1$ phases as the ground state (Figure 1). Both phases are associated with reconstructive polymorphic transformation[57] that via the 1st order structural transition connects the $P3m1$ and higher-symmetry $R3m$ phases by exchanging trigonal lattice for rhombohedral one. As illustrated in Figure 1, the reconstruction results from the shift and rotation of close-packed layers in the $[1\bar{1}0]$ crystallographic direction. Interestingly, while there is a direct option to connect the phases through the simple group-subgroup relation with index 2, it generally appears that the best choice is the polymorphic transformation with index 6. The key feature here is the full

Table 2: The base characteristics for $Ln_2OF_{2-x}Cl_xH_2$ given in terms of lattice parameters (a and c), unit cell volume (V), density (ρ), Debye temperature (Θ_D), Vickers hardness (H_V), and formation enthalpy (ΔH). The energy differences ΔE_1 and ΔE_2 describe the energetics of decomposition reactions (1a) and (1b), respectively.

X	Chem. formula	Structure	a (Å)	c (Å)	V (Å^3)	ρ (g/cm^3)	Θ_D (K)	H_V (GPa)	ΔH (kJ/mol)	ΔE_1 (kJ/mol)	ΔE_2 (kJ/mol)
0	$Y_2OF_2H_2$	P3m1	3.712	6.941	82.8	4.69	418	5.37	−1759	−18.4	+14.7
		R3m	3.657	22.014	255.1	4.57	397	4.36	−1746	−5.7	+27.4
	$La_2OF_2H_2$	P3m1	3.997	7.288	100.8	5.50	341	4.49	−1727	−2.1	+14.5
		R3m	3.978	21.444	293.9	5.66	357	4.74	−1716	+8.9	+25.5
	$Gd_2OF_2H_2$	P3m1	3.783	7.026	87.1	7.07	337	5.27	−1723	−48.8	−39.5
		R3m	3.742	21.562	261.5	7.06	329	4.47	−1709	−34.1	−24.8
1	Y_2OFClH_2	P3m1	3.735	8.181	98.8	4.20	389	3.88	−1588	−73.0	−39.9
		R3m	3.712	25.933	309.5	4.03	311	2.48	−1584	−69.3	−36.2
	La_2OFClH_2	P3m1	4.048	8.374	118.8	4.89	323	3.84	−1561	−51.5	−34.9
		R3m	4.035	25.078	353.7	4.93	284	2.79	−1553	−43.9	−27.3
	Gd_2OFClH_2	P3m1	3.812	8.181	103.1	6.23	317	3.99	−1555	−71.2	−61.9
		R3m	3.786	26.102	324.0	5.95	247	2.39	−1550	−66.2	−56.8
	$LaGdOFClH_2$	P3m1	3.939	8.292	111.4	5.49	316	3.87	−1550	−46.8	−14.4
		R3m	3.924	25.246	336.6	5.45	274	2.75	−1544	−40.5	−8.1
2	$Y_2OCl_2H_2$	R3m	3.756	30.481	372.3	3.57	248	1.59	−1385	−95.3	−62.9
	$La_2OCl_2H_2$	R3m	4.056	30.999	441.6	4.14	194	1.30	−1352	−58.2	−41.5
	$Gd_2OCl_2H_2$	R3m	3.824	30.722	389.0	5.17	193	1.45	−1353	−60.1	−50.7

occupation of the single Wyckoff positions of the $P3m1$ structure such as $1a$, $1b$ and $1c$, which in turn allows permutation relations between different ions over the lattice sites. Concerning the substitution effect, note that such "single-site" framework composed of oxophilic trivalent metal cations and anionic ligands provides a rich playground in which different anions are able to share the common chemical space within a wide range of halogen substituents. Since the $3m$ symmetry of all the occupied sites is connected with 3-fold axes of rotation parallel to [001], this factor explains why no direct structural flexibility exists between the phases. That is, before the phase transition could proceed, the unit cell of lower symmetry phase should be increased by threefold in order to afford the further self-assembly into new higher symmetry structure that will change some constraints in the stacking sequence of layers. As

also indicated in Table 1, this transformation takes place for both compositions with $x = 0$ and 1, each having low barrier energy for the corresponding atomic motions.

The quaternary hydride CaAlSiH[58] may serve as a prototypical structure for the $P3m1$ phases of Ln_2OFClH_2. Its other modification crystallizing in the $R3m$ structure can be described as the polytypical form of the $ZnIn_2S_4$ system[59,60] The crystallographic details corresponding to equilibrium geometries are given in Table 2 and Tables S1 – S17 of ESI. The trigonal ordering in both structures is characterized by a repeating sequence of two oppositely charged layers – $(LnHCl)^{+1}$ and $(LnHFO)^{-1}$ which being stacked along the main axis c are separated from each other by fluorine/chlorine atomic planes. The main feature of the halogen-coordination environment is that there exists the extra large interlayer thickness between two nearest halogen atoms. This fact implies that Coulomb forces connecting the layers along the polar direction do most significant contribution into stabilization of such columnar-type layered geometry. Note also that the estimates of density (ρ), the Debye temperature (Θ_D) and Vickers hardness (H_V) (shown in Table 2) allows us to suggest that $Ln_2OF_{2-x}Cl_xH_2$ compounds relate to usual ion-covalent solids.[45]

Stability benchmarks

We investigated the structural and dynamical stability for both $R3m$ and $P3m1$ phases of $Ln_2OF_{2-x}Cl_xH_2$ according to the following criteria. First, positive values of the squares of the zone-centered vibrational modes (given in Tables S29 – S45 of ESI) confirmed the lattice stability with respect to the relative displacements of atomic sublattices. Second, the macroscopic stability of the crystal structures has been validated by proving the total positivity of the elastic energy, which we analyzed in terms of eigenvalues of the elasticity tensor (stiffness matrix), given in Table S28 of Electronic Supplementary Information. Theoretical estimates of the formation energies, presented in the last three columns of Table 2, demonstrate the thermodynamic stability of $Ln_2OF_{2-x}Cl_xH_2$ compounds with respect to the decomposition reactions into simple elements (ΔH) as well as into binary (ΔE_1) and ternary

(ΔE_2) products.

Noncovalent bonding in the models of $Ln_2OF_{2-x}Cl_xH_2$

Topology features of valence electron density and interatomic bonding patterns are given in Figure 2 in terms of ELF. Figure 2 presents the visualization of ELF isosurfaces for two

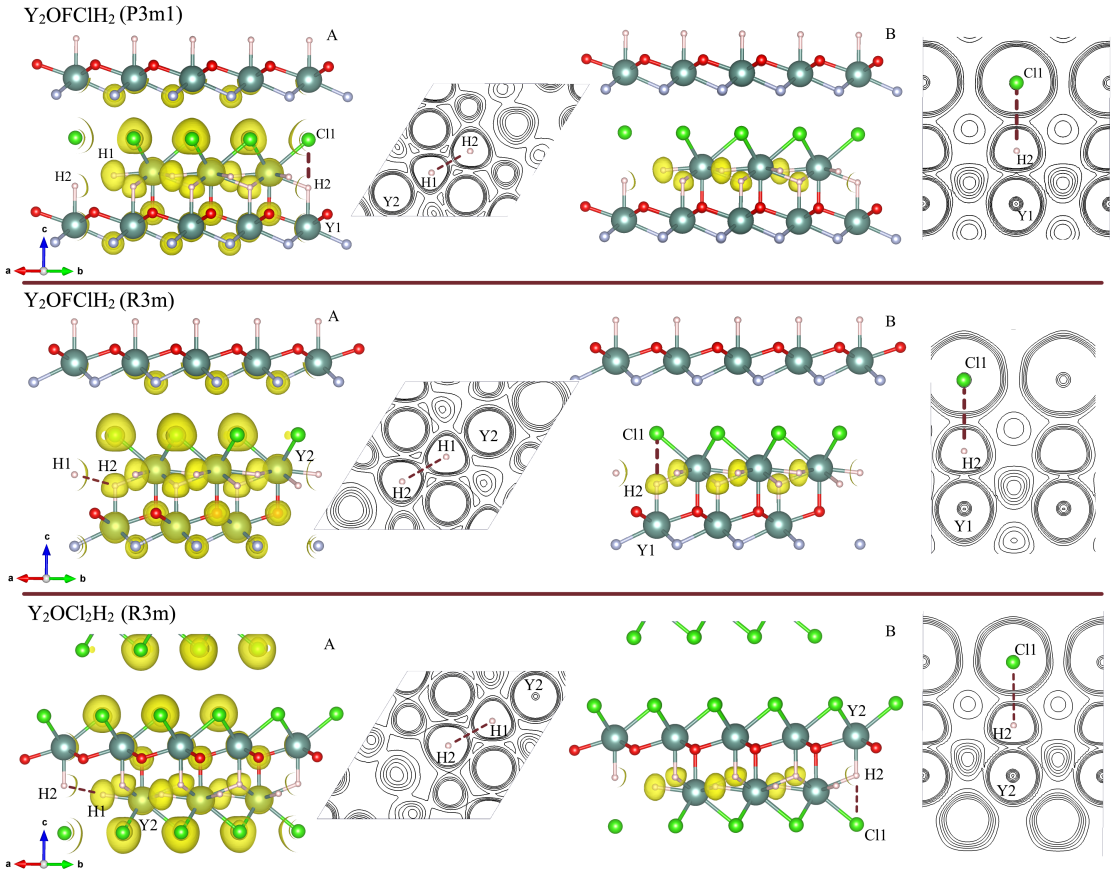

Figure 2: Schematic view on the topology of noncovalent bonding in different $Y_2OF_{2-x}Cl_xH_2$ compositions. Comparison is made in terms of graphical visualizations of charge partitioning patterns for two values of ELF: A) 0.82 (left side) and B) 0.95 (right side). The $2D$ contour plots represent the regions of valence electron density exhibiting such hydrogen bonds as Y(1)−H(2)$\cdots$Cl(1) and Y(2)−H(1)$\cdots$H(2).

values of ELF: 0.82 (Figure 2A) and 0.95 (Figure 2B). It is seen that spatial distribution of valence electron density between three anions appears significantly nonuniform. It is obvious that such variation induced by the halogenation effect may be caused by two factors. First, due to the oxophilicity of the metal cation the rigid connections with hard oxygen ligands

form the well-stabilized lattice skeleton. Secondly, comparison of electronic environments shown in Figure 2 reveals that valence electrons are most strongly localized in the region related to negatively charged hydride ion. This observation is well consistent with the classic electrostatic model of the hard ligand atom because the high Lewis basicity becomes lower for larger halogen ligands as compared with H^-.

Table 3: Benchmarks of noncovalent bonding presented in terms of anionic connectivities in $Y_2OF_{2-x}Cl_xH_2$. All lengths are given in Å.

Y−X···Z bond	X···Z	Y···X	∠Y−X···Z
$Y_2OF_2H_2$ ($R3m$)			
Y(1)−H(2)···F(1)	2.23	2.09	180.0°
Y(2)−H(1)···H(2)	2.22	2.13	169.0°
Y_2OFClH_2 ($P3m1$)			
Y(1)−H(2)···Cl(1)	2.68	2.18	180.0°
Y(2)−H(1)···H(2)	2.24	2.17	169.7°
Y_2OFClH_2 ($R3m$)			
Y(1)−H(2)···Cl(1)	2.68	2.15	180.0°
Y(2)−H(1)···H(2)	2.22	2.16	171.0°
$Y_2OCl_2H_2$ ($R3m$)			
Y(1)−H(2)···Cl(1)	2.64	2.13	180.0°
Y(2)−H(1)···H(2)	2.23	2.19	174.2°

The other feature of charge ordering in $Ln_2OF_{2-x}Cl_xH_2$ is characterized by the specific noncovalent interactions between hydrogen, fluorine and chlorine species. The mechanism that activates the anionic interactions is associated with particular crystal packing (Figure 1) whose layer configuration expands its form upon halogenation of the system. Schematic illustrations demonstrating how hydrogen bonds are mediated by active anionic species are drawn in Figure 2. Table 3 completes this figure with the geometry properties of interatomic connections evaluated for four different bulk compositions: Y_2OFClH_2 for the $P3m1$ and $R3m$ phases, and $Y_2OF_2H_2$ and $Y_2OCl_2H_2$ for the $R3m$ phase. Our results indicate that the system involves two interaction channels which are associated with H···Cl and H···H intralayer contacts, respectively (delineated as dotted lines in Figure 2). Both channels are

active inside the YHCl layer and correspond to two different bonding units: the first features vertically-directed (along polar direction) hydrid-halogen bonds, and the other, $H(2)\cdots H(1)$, – appears to be horizontally mounted between two hydrogens belonging to the nearest metal cations. In examining a dynamical stability, a matching analysis of the vibrational properties (Tables S29 – S44 of ESI) indicates that the hydrogen bonding provides additional stability to that created by the main, ion and covalent contributions. In particular, comparing high- and low-frequency modes of E and A_1 symmetries, one can note that the effect of $H(2)\cdots H(1)$ is stronger in comparison to the effect of hydrid-halogen bonds in maintaining equilibrium lattice balance.

Elastic properties of $Ln_2OF_{2-x}Cl_xH_2$

It is known[62,63] that by means of chemical engineering one could develop mechanical metamaterials with good electroelastic characteristics. A modular-type design we suggested in the present work exploits the layered symmetry of the trigonal periodic structure (presented by the $R3m$ and $P3m1$ phases) which may support the different structural arrangements composed of several anionic sites. Based on the results of computational modeling, we found an opportunity to build up the crystal packing that places the anion species at the trigonal lattice positions which are crucial for the formation of hierarchical micro-architecture similar to cellular networks of the "mechanical trusses". In other words, we showed that the intrinsic structural elements can be properly sub-assembled and configured via adaptation of anionic moduli into the specific cross-sections. This can be made by conducting chemistry of the anion substitutions and exchange.

To understand how the partial anion substitutions can modify functionality of structure–property relationships we evaluated the mechanical performance of the bulk $Ln_2OF_{2-x}Cl_xH_2$ for different levels of the anion exchange $H^- \longrightarrow F^-/Cl^-$. The calculated six (independent) elastic constants C_{ij}, presented in Table S18 of ESI, allowed us to assess the elastic macroscopic properties (Table 4). The main result is that by modifying the layered topology of

Table 4: Comparison of the mechanical properties for two phases of the bulk $Ln_2OF_{2-x}Cl_xH_2$ given in terms of elastic constants ratios, Bulk modulus (B) and volume compressibility (K). The landscape of the simulated stress fields is presented in terms of linear compressibility (β_x and β_z calculated for both crystallographic axes), projection of Young modulus (E_z), minimal and maximal values of Poisson's ratio (ν_{min} and ν_{max}).

	Chem. formula	Structure	C_{11}/C_{33}	C_{66}/C_{44}	B (GPa)	β_x (TPa^{-1})	β_z (TPa^{-1})	K (TPa^{-1})	E_z (GPa)	E_z/ρ ($GPa/g{\cdot}cm^{-3}$)	ν_{min}	ν_{max}
$x=0$	$Y_2OF_2H_2$	$P3m1$	1.25	2.07	88.3	3.2	4.9	11.3	114.1	24.34	0.05	0.60
		R3m	8.38	2.00	23.1	−0.6	44.4	43.2	18.1	3.96	−0.30	0.91
	$La_2OF_2H_2$	$P3m1$	1.24	2.38	68.4	4.1	6.3	14.6	107.7	19.59	0.11	0.55
		R3m	2.48	1.46	62.2	2.1	11.8	16.1	56.2	9.93	0.02	0.71
	$Gd_2OF_2H_2$	$P3m1$	1.24	2.07	82.9	3.4	5.2	12.1	114.6	16.22	0.09	0.55
		R3m	6.17	1.62	31.2	−0.2	32.4	32.0	23.2	3.29	−0.23	0.86
$x=1$	Y_2OFClH_2	$P3m1$	4.06	2.50	40.0	1.5	22.0	25.0	32.0	7.61	0.11	0.67
		$R3m$	8.11	9.81	18.9	2.3	48.5	53.1	18.3	4.54	0.01	0.61
	La_2OFClH_2	$P3m1$	1.82	2.50	55.6	4.1	9.7	18.0	69.8	14.26	0.06	0.53
		$R3m$	5.11	3.29	26.8	1.4	34.5	37.3	22.1	4.48	0.04	0.77
	Gd_2OFClH_2	$P3m1$	3.01	2.31	48.4	2.3	16.0	20.6	42.1	6.75	0.11	0.55
		$R3m$	8.15	9.03	18.1	2.0	51.1	55.1	17.1	2.87	0.01	0.65
	$LaGdOFClH_2$	$P3m1$	1.97	2.45	53.7	3.8	11.1	18.6	62.2	11.33	0.09	0.47
		$R3m$	5.72	3.91	24.8	1.2	37.9	40.4	20.6	3.78	0.03	0.79
$x=2$	$Y_2OCl_2H_2$	$R3m$	14.14	30.07	8.4	4.5	110.5	119.6	8.7[a]	2.44	0.01	0.77
	$La_2OCl_2H_2$	$R3m$	12.83	24.57	7.4	4.9	125.9	135.9	7.6[a]	1.84	0.01	0.75
	$Gd_2OCl_2H_2$	$R3m$	15.16	42.20	7.3	4.7	127.7	137.1	7.6[a]	1.47	0.01	0.82

[a] Can be compared with $E_z = 2.5$ GPa in the PVDF system.[61]

the unit cell via the incorporation of new anion moduli into the host pattern one can significantly change the elastic, stiffness and compressibility parameters. In the context of the mechanical strength, one can see that there exists the falling trend, connected with C_{33} and C_{44} components of the stiffness matrix, which indicates pure mechanical softening of the axial contributions into elastic degrees of freedom. Especially, reduction of the mechanical properties takes place in the $Ln_2OCl_2H_2$ compositions when the interlayer spacings of the layered geometry become larger. The other interesting thing from a chemical engineering point of view is that the halogenation affects the difference between the longitudinal and transverse components of elastic deformation for both trigonal phases. An illustrative example is given in Table 4 where we compared the anisotropy ratios C_{11}/C_{33} and C_{66}/C_{44} for

different compositions and structures.

Thus, we showed that in the $Ln_2OF_{2-x}Cl_xH_2$ system there exists the relationship between lattice micro-architecture and feasible mechanical properties. This relationship results from the presence of a structured set of diverse-anion moduli, which we simulated in terms of well-controllable modular transformations. The benefit of this modular representation is that it gives us a very useful advantage of getting softer mechanical networks within the area of stability of our model structures. In other words, we proposed to focus on altering the chemical composition in such a way when it does not disrupt the stability of the crystal lattice and does not lower lattice symmetry, yet specifically changes internal geometry of layers by forming anionic polyhedral meshes from the corner-shared anion groups. In the $3D$ perspective, this construction represents a periodic structural motif which is similar to so-called "polygonal mechanical trusses" composed of thin enforcement ribs and driven by linking nodes as hinges. Further, we argued that this way is reasonable to build a mechanical framework that may provide the macroscopic parameters such as elastic anisotropy, stiffness, and linear compressibilities with a novel functionality. As reflected in Table 4, several compositions crystallized either in the $P3m1$ or $R3m$ phases may be representative with respect to large compressibilities and spatially-dependent auxetic behaviors, the others may exhibit nontypical mechanical properties that may generate an enhancement of piezo- and electromechanical responses. For instance, the coefficient of linear compressibility has reached its maximum in $Gd_2OCl_2H_2$, $\beta_z = 127.7\ TPa^{-1}$ along the polar axis. However, because of strong anisotropy the elastic behavior is generally specific; accordingly, mechanics of the material may present various pathways for deformation-induced responses. In particular, one can predict that a transverse contraction has no sizeable effect to produce considerable values of the lateral compressibility due to strong in-plane covalent interactions. Calculations made for a full range of models of Table 4, when they were loaded in macroscopic compression, confirmed this suggestion. Moreover, two solid compositions of the $R3m$ symmetry, $Y_2OF_2H_2$ and $Gd_2OF_2H_2$, may exhibit anisotropic auxetic behavior[64–67] similar

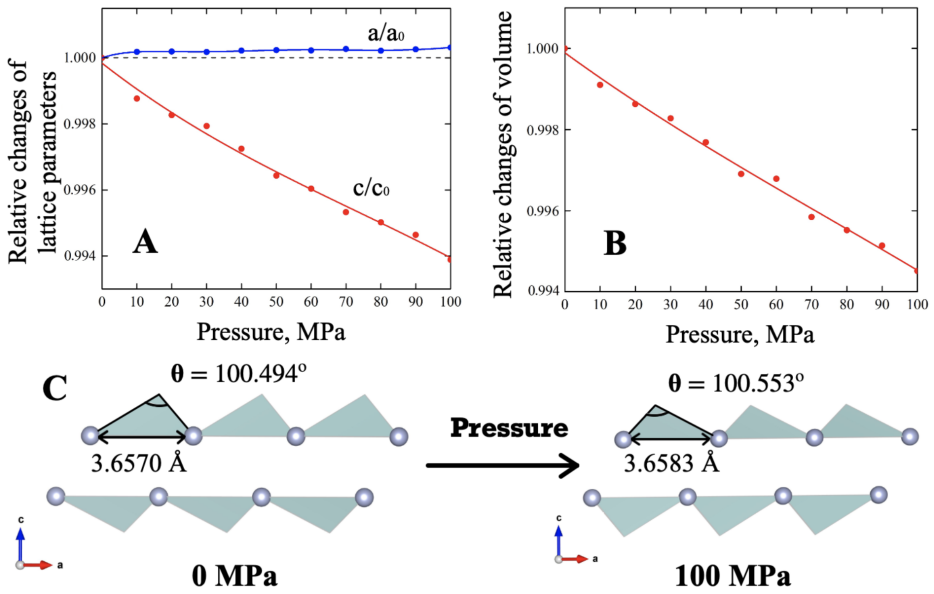

Figure 3: Geometry variation of $Y_2OF_2H_2$ micro-architecture under pressure: A) Relative changes of lattice parameters ($a_0 = 3.657$ Å and $c_0 = 22.026$ Å); B) Relative changes of unit cell volume ($V_0 = 255.1$ Å^3); C) Schematic interpretation of the nature of negative in-plane linear compressibility in terms of cooperative behaviour of YF_3 tetrahedral trusses (pictured as gray triangles). The part of inner microstructure is effectively modeled as a sandwich composed of two bonded layers. The fluorine atoms are shown by pearl balls.

to a $3D$ mechanical structure with biaxial textures, which is characterized both a negative Poisson's ratio and a negative in-plane linear compressibility (e.g., Figures S1 and S2 in ESI). In order to understand features of such deformational behavior of the bulk structure in the direction opposite to the polar axis, a series of geometric optimizations for the periodic lattice of $Y_2OF_2H_2$ were carried out for a range of compressive loads. As described briefly in Figure 3, the innate features of the deformation mechanism should be understood as a pivotal change of axial-dependent strain behaviour that is caused by the specific reshape of the force-deformation balancing[68] in the internal structure.

Piezoelectric properties

Given a set of elastic characteristics of Tables 4 and S18 of ESI, one verifies in the standard way whether the predicted materials with the softened mechanical subsystem possess the enhanced piezoelectric and electromechanical responses. One of important results of the

Table 5: Comparison of the electromechanical properties of $Ln_2OF_{2-x}Cl_xH_2$ expressed in terms of piezoelectric strain tensor d_{ij} (pC/N), piezoelectric voltage constant g_{ij} ($10^{-3}\times$[Vm/N]), piezoelectric coupling factors k_{ij} and k_t, and piezoelectric transduction coefficients $d_{ij}{\cdot}g_{ij}$ ($10^{-15}\times$[m^2/N])

Chem. formula	Structure	d_{33}	g_{33}	k_{33}	k_t	$d_{33}{\cdot}g_{33}$	d_{31}	g_{31}	k_{31}	$d_{31}{\cdot}g_{31}$	d_{15}	g_{15}	k_{15}	$d_{15}{\cdot}g_{15}$
$Y_2OF_2H_2$	P3m1	−7.72	−64.8	23.9%	8.4%	500	6.95	58.3	23.2%	405	42.80	271	53.1%	11576
	R3m	−4.64	−64.2	7.3%	3.1%	298	1.30	18.0	5.9%	23	1.34	9.3	1.9%	12
$La_2OF_2H_2$	P3m1	−2.44	−22.7	7.7%	2.8%	55	6.22	57.8	21.2%	360	32.33	210.7	37.2%	6811
	R3m	−11.77	−91.3	24.6%	17.6%	1074	3.50	27.1	10.7%	95	−3.62	−22.1	4.9%	80
Y_2OFClH_2	P3m1	−46.40	−600.0	94.4%	61.7%	27841	8.26	106.8	35.0%	882	−1.85	−14.8	2.6%	27
	R3m	−36.23	−723.3	69.3%	55.5%	26205	2.29	45.7	12.2%	105	−20.67	−177	14.6%	3663
La_2OFClH_2	P3m1	−15.12	−179.8	43.6%	33.3%	2719	5.08	60.4	18.8%	307	−0.12	−0.9	0.1%	0.1
	R3m	−52.32	−637.7	86.0%	58.9%	33367	7.68	93.6	28.2%	719	−19.56	−143.6	19.4%	2809
Gd_2OFClH_2	P3m1	−35.15	−427.5	79.5%	54.6%	15028	7.57	92.1	30.4%	697	−0.81	−6.2	1.1%	5
	R3m	−41.14	−770.9	73.7%	56.9%	31715	3.21	60.2	16.1%	193	−26.67	−221.1	18.8%	5897
$LaGdOFClH_2$	P3m1	−19.93	−238.0	54.4%	41.4%	4749	5.35	64.0	20.3%	342	−0.03	−0.2	0.1%	0.1
	R3m	−52.95	−724.3	88.9%	60.9%	38354	6.90	94.4	27.6%	651	−13.8	−91.0	12.3%	1256
$Y_2OCl_2H_2$	R3m	−10.33	−290.4	16.2%	15.7%	2999	0.37	10.4	2.1%	3.8	30.99	303.7	11.7%	9412
$La_2OCl_2H_2$	R3m	−10.03	−249.6	13.8%	12.8%	2504	0.92	22.9	4.3%	21	−30.64	−273.7	10.9%	8386
$Gd_2OCl_2H_2$	R3m	−10.61	−260.6	14.5%	14.0%	2765	0.49	12.0	2.5%	6	−21.36	−196.1	6.4%	4188

current paper is that we suggested two series of such materials, Ln_2OFClH_2 and $Ln_2OCl_2H_2$, which demonstrate a high level of coupling between elastic and electrical degrees of freedom. As indicated in Table 5, the comparison of theoretical values, for example such as d_{33} components of piezoelectric strain tensor, piezoelectric voltage constants g_{33} and g_{15}, and piezoelectric coupling factors k_{33}, shows that a number of compounds exhibit both high voltage sensitivity and remarkable piezoelectric output voltage. For the Ln_2OClFH_2 systems, the general contrast-matching analysis of the open circuit voltage and harvested power density with respect to the corresponding characteristics of lead-free piezoceramics, piezoelectric semiconductor ZnO and piezopolymer PVDF can be found in Table S49 of ESI.

Thus, unique architecture represented by the models of Table 5 offers the capability to make electro-active elastic dielectrics with sensing characteristics greater than those of PVDF electroactive piezopolymer. The major differences concerning the practical uses can be seen from the comparison of dielectric, piezoelectric, and electro-mechanical characteris-

tics. The first fact is that the predicted compounds $Ln_2OF_{2-x}Cl_xH_2$ can be classified as solid materials that in relation to E_z/ρ ratio may be similar to a lightweight mechanical metamaterial. Chemically, they relate to the group of lead-free piezoelectrics-semiconductors like ZnO and AlN among which some of them may exhibit the anomalously large level of the linear compression along the polar c-axis. Secondly, due to the high voltage sensitivity and the moderate piezoelectric output voltage, some of these models have a number of advances for the development of transverse stress sensing elements for a wide range of applied mechanical loading up to 60 MPa (e.g., Figure 3). The key advantage is that they could operate under thermal heating conditions, in radiation fields or other aggressive environments that are beyond out of scope of polymer piezoelements. Moreover, Ln_2OFClH_2 crystallized in the $R3m$ phase may find applications as a functional unit of the energy conversion system[69–71] that being integrated into the hard road surfaces can harvest the energy of transverse mechanical loads. Thirdly, the feature to produce large strains along the mechanically soft polar axis is of practical interest for the use in a dielectric actuator as a passive film (similar to elastomer) placed between the dissimilar electrodes. Qualitative model estimates showed that we could expect to achieve the resonant frequencies in the range of 100 Hz to 1 kHz.

Conclusions

The emphasis of our research work was made on some aspects of anion chemistry of mixed-anion crystalline system that deal with varying anion content in terms of stability, charge distributions, and bonding configurations. The key idea was to effectively manage the microstructure-properties relationships via the interplay of anionic degrees of freedom in a polar crystalline medium. The central attention was paid to the geometry of partial substitutions in heteroatomic anion $[OF_{2-x}Cl_xH_2]^{6-}$. In the context of mechanical behaviour, this allowed us to accurately simulate the modification of elastic properties through the flexibility of new anionic connections. In the present study, we suggested the models of

the polar solid-state material $Ln_2OF_{2-x}Cl_xH_2$ (Ln = Y, La, Gd) which demonstrates unique combination of the elastic and electromechanical properties. This opens a new way in the development of the advanced energy harvesting devices that may combine high piezoelectric output with the softness of PVDF-type piezopolymers from the one hand and the thermal and mechanical stability of hard piezoceramic elements from the other hand. Moreover, the predicted materials may be of particular interest for the design of the following electromechanical devices: (i) transverse stress sensing elements for the control of applied mechanical loads, (ii) sensitive tactile sensors operating in the range of external forces from 0.01 to 1000 N, and (iii) a responsive component of artificial skin models. Moreover, our conceptual estimates of the efficiency of energy harvesting showed that the piezoelectric harvesting power density produced by several Ln_2OClFH_2 systems may be about 5–10 times larger than that of commercially available PZT-5H ceramics and about 3–4 times larger than that of piezoelectric polymers.

Supporting Information Available

Electronic Supplementary Information (ESI) available: [details of any supplementary information available should be included here]. See DOI: 00.0000/00000000.

References

(1) Kageyama, H.; Hayashi, K.; Maeda, K.; Attfield, J.; Hiroi, Z.; Rondinelli, J.; Poeppelmeier, K. Expanding frontiers in materials chemistry and physics with multiple anions. *Nature Communications* **2018**, *9*, 204–209.

(2) Takeiri, F.; Kageyama, H. Mixed-Anion Compounds: A New Trend in Solid State Chemistry. *Nihon Kessho Gakkaishi* **2018**, *60*, 240–245.

(3) Fokin, V.; Malov, Y.; Fokina, E.; Troitskaya, S.; Shilkin, S. Investigation of interactions in the TiH_2-O_2 system. *International Journal of Hydrogen Energy* **1995**, *20*, 387 – 389.

(4) Fokin, V.; Malov, Y.; Fokina, E.; Shilkin, S. Study of the phase-forming features in the ZrH_2-O_2 system. *International Journal of Hydrogen Energy* **1996**, *21*, 969–973.

(5) Hosono, H.; Matsuishi, S. Superconductivity induced by hydrogen anion substitution in 1111-type iron arsenides. *Current Opinion in Solid State and Materials Science* **2013**, *17*, 49 – 58, Fe-based Superconductors.

(6) Hayward, M. A.; Cussen, E. J.; Claridge, J. B.; Bieringer, M.; Rosseinsky, M. J.; Kiely, C. J.; Blundell, S. J.; Marshall, I. M.; Pratt, F. L. The Hydride Anion in an Extended Transition Metal Oxide Array: LaSrCoO3H0.7. *Science* **2002**, *295*, 1882–1884.

(7) Iimura, S.; Matuishi, S.; Sato, H.; Hanna, T.; Muraba, Y.; Wng Kim, S.; Eun Kim, J.; Takata, M.; Hosono, H. Two-Dome Structure in Electron-Doped Iron Arsenide Superconductors. *Nature communications* **2012**, *3*, 943.

(8) Yajima, T.; Kitada, A.; Kobayashi, Y.; Sakaguchi, T.; Bouilly, G.; Kasahara, S.; Terashima, T.; Takano, M.; Kageyama, H. Epitaxial Thin Films of ATiO3–xHx (A = Ba, Sr, Ca) with Metallic Conductivity. *Journal of the American Chemical Society* **2012**, *134*, 8782–8785, PMID: 22563869.

(9) Kobayashi, Y.; Hernandez, O.; Tassel, C.; Kageyama, H. New chemistry of transition metal oxyhydrides. *Science and Technology of Advanced Materials* **2017**, *18*, 905–918.

(10) Yamamoto, T.; Kageyama, H. Hydride Reductions of Transition Metal Oxides. *Chemistry Letters* **2013**, *42*, 946–953.

(11) Jacob, K. T.; Saji, V. S.; Waseda, Y. Lanthanum Oxyfluoride: Structure, Stability,

and Ionic Conductivity. *International Journal of Applied Ceramic Technology* **2006**, *3*, 312–321.

(12) Mann, A. W.; Bevan, D. J. M. The crystal structure of stoichiometric yttrium oxyfluoride, YOF. *Acta Crystallographica Section B* **1970**, *26*, 2129–2131.

(13) Melnichenko, E.; Gorbenko, O.; Laptash, N.; Polyshchuk, S. Solid transition metal oxyfluorides. *Journal of Fluorine Chemistry* **1989**, *45*, 52.

(14) Kobayashi, Y.; Tian, M.; Eguchi, M.; Mallouk, T. E. Ion-exchangeable, electronically conducting layered perovskite oxyfluorides. *Journal of the American Chemical Society* **2009**, *131*, 9849—9855.

(15) Mongstad, T.; Platzer-Björkman, C.; Maehlen, J. P.; Mooij, L. P.; Pivak, Y.; Dam, B.; Marstein, E. S.; Hauback, B. C.; Karazhanov, S. Z. A new thin film photochromic material: Oxygen-containing yttrium hydride. *Solar Energy Materials and Solar Cells* **2011**, *95*, 3596 – 3599.

(16) Baba, E. M.; Montero, J.; Strugovshchikov, E.; Zayim, E. O.; Karazhanov, S. Light-induced breathing in photochromic yttrium oxyhydrides. *Phys. Rev. Materials* **2020**, *4*, 025201.

(17) Pishtshev, A.; Karazhanov, S. Z. Role of oxygen in materials properties of yttrium trihydride. *Solid State Communications* **2014**, *194*, 39 – 42.

(18) Pishtshev, A.; Strugovshchikov, E.; Karazhanov, S. Conceptual Design of Yttrium Oxyhydrides: Phase Diagram, Structure, and Properties. *Crystal Growth & Design* **2019**, *19*, 2574–2582.

(19) Pishtshev, A.; Strugovshchikov, E. Computational Prediction of Ferro- and Piezoelectricity in Lead-Free Oxyhydrides Ln2H4O (Ln = Y, La). *Advanced Theory and Simulations* **2019**, *2*, 1900144.

(20) Montero, J.; Martinsen, F. A.; García-Tecedor, M.; Karazhanov, S. Z.; Maestre, D.; Hauback, B.; Marstein, E. S. Photochromic mechanism in oxygen-containing yttrium hydride thin films: An optical perspective. *Phys. Rev. B* **2017**, *95*, 201301.

(21) Nafezarefi, F.; Schreuders, H.; Dam, B.; Cornelius, S. Photochromism of rare-earth metal-oxy-hydrides. *Applied Physics Letters* **2017**, *111*, 103903.

(22) H. Rude, L.; Filsø, U.; D'Anna, V.; Spyratou, A.; Richter, B.; Hino, S.; Zavorotynska, O.; Baricco, M.; Sørby, M.; Hauback, B.; Hagemann, H.; Besenbacher, F.; Skibsted, J.; Jensen, T. Hydrogen–fluorine exchange in NaBH4–NaBF4. *Phys. Chem. Chem. Phys.* **2013**, *15*.

(23) R, V.; Ravindran, P. Phase Stability, Phase Mixing and Phase Separation in Fluorinated Alkaline Earth Hydrides. *The Journal of Physical Chemistry C* **2017**, *121*.

(24) Castro, J.; Yavari, A.; LeMoulec, A.; Ishikawa, T.; Botta, W. Improving H-sorption in MgH2 powders by addition of nanoparticles of transition metal fluoride catalysts and mechanical alloying. *Journal of Alloys and Compounds* **2005**, *389*, 270–274.

(25) Deledda, S.; Borissova, A.; Poinsignon, C.; Botta, W.; Dornheim, M.; Klassen, T. H-Sorption in MgH2 Nanocomposites Containing Fe or Ni with Fluorine. *Cheminform* **2006**, *37*.

(26) Aleksandrov, K. S.; Beznosikov, B. V. Architecture and properties of perovskite-like crystals. *Ferroelectrics* **1999**, *226*, 1–9.

(27) Beznosikov, B. V.; Aleksandrov, K. S. Layered Perovskite-Like Crystals with (A1+C1) Stacks in the Structure. *Journal of Structural Chemistry* **2000**, *41*, 1004–1008.

(28) Beznosikov, B. V.; Aleksandrov, K. S. Prediction of Pra-Phases of Layered Perovskite-Like Structures with Cation Vacancies. *Journal of Structural Chemistry* **2002**, *43*, 172–175.

(29) Aleksandrov, K. S.; Beznosikov, B. V. *Possible new phases in layered perovskite-like crystals (crystal-chemical prognosis)*; Preprint 813F, 2002.

(30) Jiang, X. et al. Isotropic Negative Area Compressibility over Large Pressure Range in Potassium Beryllium Fluoroborate and its Potential Applications in Deep Ultraviolet Region. *Advanced Materials* **2015**, *27*, 4851–4857.

(31) Perdew, J. P.; Burke, K.; Ernzerhof, M. Generalized Gradient Approximation Made Simple. *Phys. Rev. Lett.* **1996**, *77*, 3865–3868.

(32) Kresse, G.; Hafner, J. Ab initio molecular dynamics for liquid metals. *Phys. Rev. B* **1993**, *47*, 558–561.

(33) Kresse, G.; Furthmüller, J. Efficient iterative schemes for ab initio total-energy calculations using a plane-wave basis set. *Phys. Rev. B* **1996**, *54*, 11169–11186.

(34) Blöchl, P. E. Projector augmented-wave method. *Phys. Rev. B* **1994**, *50*, 17953–17979.

(35) Kresse, G.; Joubert, D. From ultrasoft pseudopotentials to the projector augmented-wave method. *Phys. Rev. B* **1999**, *59*, 1758–1775.

(36) Dudarev, S. L.; Botton, G. A.; Savrasov, S. Y.; Humphreys, C. J.; Sutton, A. P. Electron-energy-loss spectra and the structural stability of nickel oxide: An LSDA+U study. *Phys. Rev. B* **1998**, *57*, 1505–1509.

(37) Topsakal, M.; Wentzcovitch, R. Accurate projected augmented wave (PAW) datasets for rare-earth elements (RE=La–Lu). *Comput. Mater. Sci.* **2014**, *95*, 263–270.

(38) Becke, A. D.; Edgecombe, K. E. A simple measure of electron localization in atomic and molecular systems. *The Journal of Chemical Physics* **1990**, *92*, 5397–5403.

(39) Savin, A.; Jepsen, O.; Flad, J.; Andersen, O. K.; Preuss, H.; von Schnering, H. G. Electron Localization in Solid-State Structures of the Elements: the Diamond Structure. *Angew. Chem. Int. Ed.* **1992**, *31*, 187–188.

(40) Momma, K.; Izumi, F. VESTA 3 for Three-Dimensional Visualization of Crystal, Volumetric and Morphology Data. *Journal of Applied Crystallography* **2011**, *44*.

(41) Gaillac, R.; Pullumbi, P.; Coudert, F.-X. ELATE: an open-source online application for analysis and visualization of elastic tensors. *Journal of Physics: Condensed Matter* **2016**, *28*, 275201.

(42) Gaillac, R.; Coudert, F.-X. ELATE: Elastic tensor analysis. `http://progs.coudert.name/elate`.

(43) Paufler, P. J. F. Nye. Physical Properties of Crystals. Clarendon Press — Oxford. First published in paperback with corrections and new material 1985. XVII + 329 p. £ 15.00. ISBN 0-19-851165-5. *Crystal Research and Technology* **1986**, *21*, 1508–1508.

(44) Anderson, O. L. A simplified method for calculating the debye temperature from elastic constants. *J. Phys. Chem. Solids* **1963**, *24*, 909 – 917.

(45) Mazhnik, E.; Oganov, A. R. A model of hardness and fracture toughness of solids. *Journal of Applied Physics* **2019**, *126*, 125109.

(46) Ivantchev, S.; Kroumova, E.; Madariaga, G.; Pérez-Mato, J. M.; Aroyo, M. I. *SUBGROUPGRAPH*: a computer program for analysis of group–subgroup relations between space groups. *J. Appl. Crystallogr.* **2000**, *33*, 1190–1191.

(47) Kroumova, E.; Aroyo, M. I.; Pérez-Mato, J. M.; Kirov, A.; Capillas, C.; Ivantchev, S.; Wondratschek, H. Bilbao Crystallographic Server I: Databases and crystallographic computing programs. *Phase Transitions* **2003**, *76*, 155–170.

(48) Bilbao Crystallographic Server. `http://www.cryst.ehu.es`.

(49) Aroyo, M.; Pérez-Mato, J.; Orobengoa, D.; Tasci, E.; de la Flor, G.; Kirov, A. Crystallography online: Bilbao Crystallographic Server. *Bulg. Chem. Commun.* **2011**, *43*, 183–197.

(50) Aroyo, M.; Pérez-Mato, J.; Capillas, C.; Kroumova, E.; Ivantchev, S.; Madariaga, G.; Kirov, A.; Wondratschek, H. Bilbao Crystallographic Server I: Databases and crystallographic computing programs. *Z. Krist.* **2006**, *221*, 15–27.

(51) Aroyo, M. I.; Kirov, A.; Capillas, C.; Pérez-Mato, J. M.; Wondratschek, H. Bilbao Crystallographic Server. II. Representations of crystallographic point groups and space groups. *Acta Cryst.* **2006**, *A62*, 115–128.

(52) Gajdoš, M.; Hummer, K.; Kresse, G.; Furthmüller, J.; Bechstedt, F. Linear optical properties in the projector-augmented wave methodology. *Phys. Rev. B* **2006**, *73*, 045112.

(53) Liang, J.; Liao, W. Impedance analysis for piezoelectric energy harvesting devices under displacement and force excitations. The 2010 IEEE International Conference on Information and Automation. 2010; pp 42–47.

(54) Liang, J.; Liao, W.-H. Impedance matching for improving piezoelectric energy harvesting systems. *Proceedings of SPIE - The International Society for Optical Engineering* **2010**, *7643*.

(55) Bowen, C. R.; Topolov, V. Y.; Kim, H. A. *Modern Piezoelectric Energy-Harvesting Materials*, 1st ed.; 2016.

(56) Bhugra, H.; Piazza, G. *Piezoelectric MEMS Resonators*, 1st ed.; 2017.

(57) Müller, U. *Symmetry Relationships between Crystal Structures: Applications of Crystallographic Group Theory in Crystal Chemistry*; Oxford University Press, 2013.

(58) Björling, T.; Noréus, D.; Jansson, K.; Andersson, M.; Leonova, E.; Edén, M.; Hålenius, U.; Häussermann, U. SrAlSiH: A Polyanionic Semiconductor Hydride. *Angewandte Chemie International Edition* **2005**, *44*, 7269–7273.

(59) Lappe, F.; Niggli, A.; Nitsche, R.; White, J. G. The crystal structure of In_2ZnS_4. *Z. Kristallogr.* **1962**, *117*, 146–152.

(60) Berand, N.; Range, K.-J. A redetermination of the crystal structure of the (III)a-polytypic form of diindium zinc tetrasulfide, ZnIn2S4. *J. Alloys Compd.* **1994**, *205*, 295–301.

(61) Zhang, Q.; Bharti, V.; Kavarnos, G. *Encyclopedia of Smart Materials*; American Cancer Society, 2002.

(62) Zadpoor, A. A. Mechanical meta-materials. *Materials Horizons* **2016**, *3*, 371–381.

(63) Shu, L.; Liang, R.; Yu, Y.; Tian, T.; Rao, Z.; Wang, Y. Unique elastic, dielectric and piezoelectric properties of micro-architected metamaterials. *Journal of Materials Chemistry C* **2019**, *7*, 2758–2765.

(64) Lakes, R. Materials with structural hierarchy. *Nature* **1993**, *361*, 511–515.

(65) Xinchun, S.; Lakes, R. S. Stability of elastic material with negative stiffness and negative Poissons ratio. *physica status solidi (b)* **2007**, *244*, 1008–1026.

(66) Lakes, R. S. Piezoelectric composite lattices with high sensitivity. *Philosophical Magazine Letters* **2013**, *94*, 37–44.

(67) Spagnoli, A.; Brighenti, R.; Lanfranchi, M.; Soncini, F. On the Auxetic Behaviour of Metamaterials with Re-entrant Cell Structures. *Procedia Engineering* **2015**, *109*, 410 – 417, XXIII Italian Group of Fracture Meeting, IGFXXIII.

(68) Lakes, R.; Rosakis, P.; Ruina, A. Microbuckling instability in elastomeric cellular solids. *Journal of Materials Science* **1993**, *28*, 4667–4672.

(69) Harris, P.; Arafa, M.; Litak, G.; Bowen, C. R.; Iwaniec, J. Output response identification in a multistable system for piezoelectric energy harvesting. *The European Physical Journal B* **2017**, *90*, 20.

(70) Hadas, Z.; Janak, L.; Smilek, J. Virtual prototypes of energy harvesting systems for industrial applications. *Mechanical Systems and Signal Processing* **2018**, *110*, 152 – 164.

(71) Tang, X.; Wang, X.; Cattley, R.; Gu, F.; Ball, A. Energy Harvesting Technologies for Achieving Self-Powered Wireless Sensor Networks in Machine Condition Monitoring: A Review. *Sensors* **2018**, *18*, 4113.